Faradaurate-940: Synthesis, Mass Spectrometry, Electron Microscopy, High-Energy X-ray Diffraction, and X-ray Scattering Study of $Au_{\sim 940\pm 20}(SR)_{\sim 160\pm 4}$ Nanocrystals

Chanaka Kumara,[†] Xiaobing Zuo,[‡] David A. Cullen,[§] and Amala Dass[†,*]

[†]Department of Chemistry and Biochemistry, University of Mississippi, Oxford, Mississippi 38677,United States, [‡]X-ray Science Division, Advanced Photon Source, Argonne National Laboratory, Argonne, Illinois 60439, United States, and [§]Materials Science and Technology Division, Oak Ridge National Laboratory, Oak Ridge, Tennessee 37831, United States

ABSTRACT Obtaining monodisperse nanocrystals and determining their composition to the atomic level and their atomic structure is highly desirable but is generally lacking. Here, we report the discovery and comprehensive characterization of a 2.9 nm plasmonic nanocrystal with a composition of $Au_{940\pm 20}(SCH_2CH_2Ph)_{160\pm 4}$, which is the largest mass spectrometrically characterized gold thiolate nanoparticle produced to date. The compositional assignment has been made using electrospray ionization and matrix-assisted laser desorption ionization mass spectrometry (MS). The MS results show an unprecedented size monodispersity, where the number of Au atoms varies by only 40 atoms (940 ± 20). The mass spectrometrically determined composition and size are supported by aberration-corrected scanning transmission electron microscopy (STEM) and synchrotron-based methods such as atomic pair distribution function (PDF) and small-angle X-ray scattering (SAXS). Lower-resolution STEM images show an ensemble of particles—1000s per frame—visually demonstrating monodispersity. Modeling of SAXS data on statistically significant nanoparticle population—approximately 10^{12} individual nanoparticles—shows that the diameter is 3.0 ± 0.2 nm, supporting mass spectrometry and electron microscopy results on monodispersity. Atomic PDF based on high-energy X-ray diffraction experiments shows decent match with either a Marks decahedral or truncated octahedral structure. Atomic resolution STEM images of single particles and their fast Fourier transform suggest face-centered cubic arrangement. UV−visible spectroscopy data show that Faradaurate-940 supports a surface plasmon resonance peak at ~505 nm. These monodisperse plasmonic nanoparticles minimize averaging effects and have potential application in solar cells, nano-optical devices, catalysis, and drug delivery.

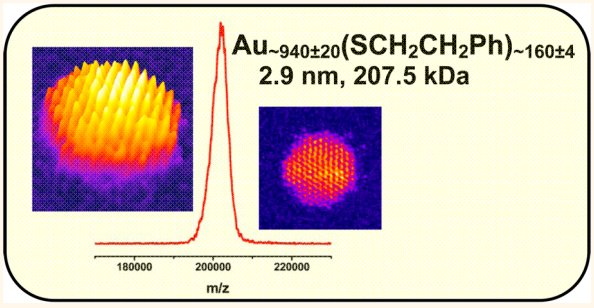

KEYWORDS: nanoclusters · monolayer-protected clusters · atomic PDF

Gold nanoparticles are used in catalysis, energy harvesting, nanodevices, drug delivery, and biomedical applications. However, colloidal gold nanoparticles, in general, suffer from the lack of stability, resulting in aggregation upon removal of solvent, and poor monodispersity, leading to averaging effects due to many particle sizes and shapes. Thiolated gold nanoparticles show excellent monodispersity and stability. In the ultrasmall <2 nm size regime, they form atomically monodisperse molecules (nanomolecules), such as $Au_{25}(SR)_{18}$,[1] $Au_{38}(SR)_{24}$,[2] $Au_{40}(SR)_{24}$,[3] $Au_{130}(SR)_{50}$,[4] and $Au_{144}(SR)_{60}$[5] (see Scheme 1). Salient features include (a) the compositional assignment by MS; (b) X-ray crystallographic structure determination of many sizes yielding core shape and exact Au−SR interfacial structure; (c) rich size-dependent optical and electrochemical properties;[6,7] (d) the ability to manipulate the core by alloying[8,9] and outer thiol monolayer by ligand exchange;[10,11] (e) high stability in solution and dry form, under ambient environmental conditions and elevated temperatures, 80 °C. Pioneering crystallographic structure reports include

* Address correspondence to amal@olemiss.edu.

Received for review April 8, 2014 and accepted May 12, 2014.

Published online May 12, 2014
10.1021/nn501970v

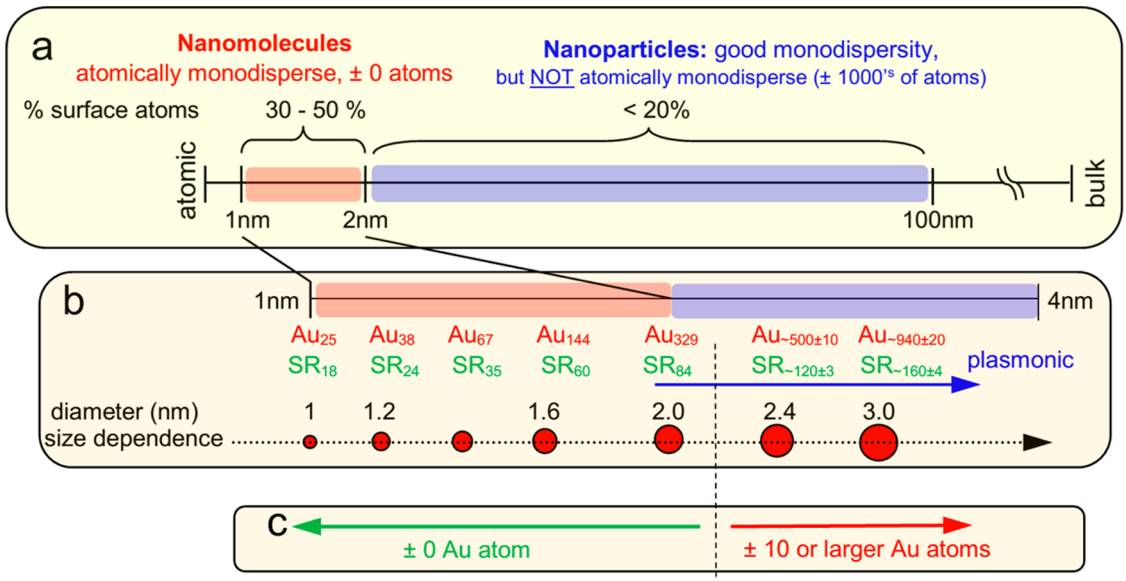

Scheme 1. Gold nanomolecules, plasmonic Faradaurates, and nanoparticles. (a) The 1−100 nm size regime with nanomolecules (±0 Au atom variation) in the 1−2 nm region and nanoparticles in the 2−100 nm regime (where very good monodispersity has been achieved, but the size distribution is still ±1000s of atoms or a few nanometers). (b) Thiolated gold nanomolecules, such as Au_{25}, Au_{38}, Au_{67}, Au_{144}, and Au_{329} with a precise number of metal atoms and organic ligands and $Au_{\sim 500\pm 10}(SR)_{\sim 120\pm 3}$ and $Au_{\sim 940\pm 20}(SR)_{\sim 160\pm 4}$. Only highly reproducible and phenylethane thiol-protected Au cores are shown. (c) Dashed line, between 329 and 500 atom sizes, indicating the transition between the fixed composition containing nanomolecules region, with ±0 Au atom variation *versus* polydisperse $Au_{\sim 500\pm 10}(SR)_{\sim 120\pm 3}$ particles with a ±10 Au atom variation. The title Faradaurate-940 has a variation of ±20 Au atom with a composition of $Au_{\sim 940\pm 20}(SR)_{\sim 160\pm 4}$.

$Au_{102}(S-C_6H_4-COOH)_{44}$[12] and $Au_{25}(SCH_2CH_2Ph)_{18}$.[1] The most important techniques used in nanomolecule-based research are mass spectrometry (MS) and X-ray crystallography. Complementary and supporting evidence for the nanomolecules (±0 atom variation) in the form of commonly used nanoparticle characterization methods such as transmission electron microscopy (TEM), small-angle X-ray scattering (SAXS), and X-ray powder diffraction is, in general, lacking.

In general, there is a vast difference in size determination and characterization of gold thiolate nanomolecules (atomically monodisperse molecules such as $Au_{25}(SR)_{18}$, $Au_{38}(SR)_{24}$, $Au_{144}(SR)_{60}$) and gold nanoparticles whose diameter is larger than 5 nm (see Scheme 1). The powerful characterization tools in the study of nanomolecules (<2 nm) are mass spectrometry and X-ray crystallography. While in the latter case, >5 nm gold nanoparticles are commonly characterized by TEM, X-ray diffraction, SAXS, and other techniques. Generally, there is a sense of disbelief or lack of complete confidence in the nanomolecule research results by the researchers in the wider >5 nm nanoparticle research community. This is rightfully so because if one makes atomically monodisperse gold molecules (*i.e.*, nanomolecules) then the monodispersity has to be corroborated by TEM, SAXS, and other commonly used nanoparticle analysis methods. However, performing electron microscopy on ultrasmall nanomolecules can alter the size, composition, and atomic structure due to beam damage.[13] Here, for the first time, we support the mass spectrometrically determined composition and size with scanning transmission electron microscopy (STEM) and synchrotron-based methods such as atomic pair distribution function (PDF) and SAXS.

Extensive efforts have been made to synthesize and characterize monodisperse plasmonic nanoparticles at sizes smaller than 5 nm.[14,15] However, the generation of superstable plasmonic nanoparticles with defined composition is hindered by the lack of suitable synthesis, isolation, and purification protocols. Recently, we have reported the 76.3 kDa superstable plasmonic nanoparticle.[16] Named Faradaurate, in honor of Michael Faraday,[17] this atomically monodisperse plasmonic molecule contains exactly 329 gold atoms and 84 ligands.[18] We mentioned in this work the existence of other stable sizes at 115 and 207 kDa.

Here we report the synthesis, isolation, and characterization of highly stable, monodisperse, and plasmonic nanoparticles whose composition is $Au_{\sim 940}(SR)_{\sim 160}$. With an unprecedented leap in the mass range of nanoparticle mass spectrometry, we report the electrospray ionization mass spectrometry (ESI-MS) of a 207 kDa nanoparticle. This paper describes the largest mass spectrometrically characterized thiolated gold nanoparticles to date. The monodispersity and size distribution shown by mass spectrometry was supported by other standard nanoparticle characterization methods, including electron microscopy and SAXS, which is generally lacking in research on nanomolecules. The STEM studies on the Faradaurate-940 is made possible due in part to the enhanced stability due to the larger size of the

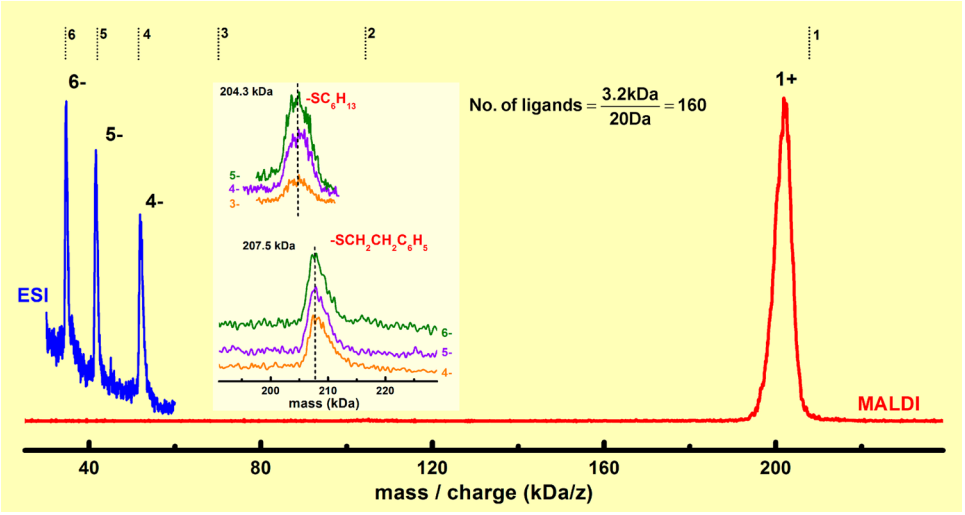

Figure 1. Mass spectrometry. MALDI (red) and ESI (blue) mass spectra of 207 kDa nanoparticles synthesized using $HSCH_2CH_2Ph$ thiol. MALDI-MS with DCTB matrix shows 1+ ions, while ESI-MS yields 4−, 5−, and 6− multiply charged ions. The theoretical values for charge states 1, 2, 3, 4, 5, and 6 are shown by dotted lines at the top. The inset shows the deconvoluted ESI mass spectra of 940 atom nanoparticles protected by $-SC_6H_{13}$ and $-SCH_2CH_2Ph$. The deconvolution of the multiply charged ions (4−, 5−, and 6− ESI peaks are multiplied by 4, 5, and 6, respectively, to yield the 1− molecular ion at 207.5 kDa for the $-SCH_2CH_2Ph$ ligand) of the multiply charged ions. This mass difference was used to calculate the number of ligands. The composition of the nanoparticles was determined to be $Au_{940\pm20}(SR)_{160\pm4}$.

940 atom species when compared with the <329 atom nanomolecules. Atomic resolution STEM images and fast Fourier transform (FFT) pattern suggest that the particle has a cubic closed-packed face-centered cubic (fcc) atomic arrangement. This is distinct from the non-crystallographic icosahedral and Marks decahedral cores of smaller than 329 atom nanomolecules protected by phenylethanethiol ligands.

RESULTS AND DISCUSSION

Mass Spectrometry. Figure 1 shows the matrix-assisted laser desorption ionization (MALDI) and ESI-MS of the 200 kDa nanoparticles synthesized using phenylethanethiol. MALDI-MS (red curve) obtained using a DCTB matrix[19] shows a single peak at ~200 kDa, showing the purity of the title nanoparticles. Supporting Information Figure S1 shows the MALDI spectra in the 30 to 500 kDa range, showing the absence of both smaller and larger nanoparticles. The broad peak in MALDI with a full width at half-maximum (fwhm) of 6 kDa is due to the resolution limit of the time-of-flight (TOF) tube and fragmentation due to the incident laser energy. Therefore, electrospray ionization mass spectrometry, a softer ionization technique when compared with MALDI-MS, was employed to determine the composition without fragmentation. Figure 1 (blue) shows the electrospray ionization mass spectrometry with multiply charged peaks at 51.8, 41.6, and 34.6 kDa which correspond to the highest points of the 4−, 5−, and 6− molecular ions. The deconvolution of these multiply charge peaks (multiplying the 4−, 5−, and 6− peaks with 4, 5, and 6, respectively) resulted in peaks all centering at 207.5 kDa, as shown in the Figure 1 inset. This suggests that the three ESI peaks all correspond to the same MALDI peak at ~200 kDa but are present with different number of charges. The initial compositional assignment was made by ESI-MS to be $Au_{\sim940}(SR)_{\sim160}$. However, further compositional verification was made by synthesizing the $Au_{\sim940}(SR)_{\sim160}$ with a second thiol (hexanethiol) using the same synthetic protocol. The molecular weight of phenylethanethiol, $C_6H_5CH_2CH_2SH$, and hexanethiol, $C_6H_{13}SH$, is 138 and 118 Da, respectively. The difference in the ligand mass, 20 Da, was first used to assign the total number of ligands, 160. From the ligand count, the number of gold atoms was back-calculated. This method of assigning the composition of a newly synthesized nanoparticle by determining the mass difference of nanoparticles prepared using two different ligands in order to assign the composition was successfully used by several research groups.[4,20,21] Deconvoluting the multiply charged peaks to the molecular 1− ion leads to a width of 8250 Da. The extreme case, where the entire 8250 Da difference corresponds to Au atoms, would lead to a variation of 40 Au atoms or 940 ± 20. If the entire mass is due to ligands, then it would lead to a variation of 60 $C_6H_5CH_2CH_2SH$ ligands. We calculate the percent variation of Au atoms (40/940 = 4.2%) and apply it to the ligand to account for ligand variation. This would lead to a reasonable variation of (160 × 0.042 = 6.8) seven ligands. Finally, we conclude that the composition of the title compound to be $Au_{\sim940\pm20}(SR)_{\sim160\pm4}$. Control experiments were performed to ensure that fragmentation was minimized. For example, under identical conditions, the multiply charged peaks $Au_{329}(SR)_{84}$ and $Au_{144}(SR)_{60}$ in the 30−40 kDa/z range yield sharp peaks, with fwhm of 30 Da, suggesting that these 329 and 144 atom species contain one species (± 0 Au atom variation).

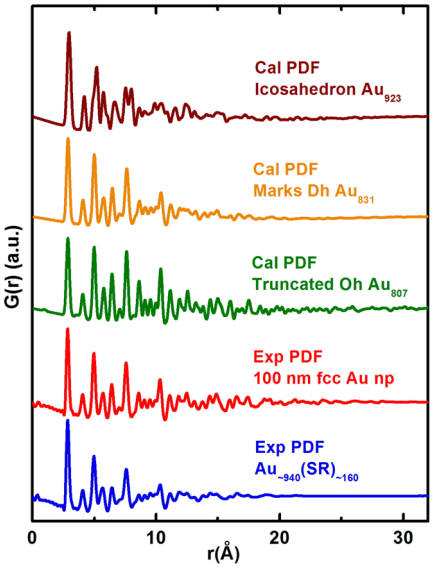

Figure 2. Atomic PDF of $Au_{\sim 940}(SCH_2CH_2Ph)_{\sim 160}$ in comparison with naked commercially available 100 nm fcc-like nanoparticles. The calculated PDF of icosahedral Au_{923}, Marks decahedral Au_{831}, and truncated octahedral Au_{807} is also included. Based on atomic PDF alone, it is not possible to distinguish between decahedral *versus* fcc atomic structure.

The broad peak (fwhm of 8250 Da for the deconvoluted 1− peak) raises the question if the electrosprayed Faradaurate-940 ions are accompanied by solvent molecules. The desolvation temperature in the ESI source was 200 °C. Control experiments using $Au_{144}(SR)_{60}$ and $Au_{329}(SR)_{84}$ under identical conditions show no additional broadening of the peaks, suggesting the absence of solvent molecules. We also performed other control experiments where the $Au_{329}(SR)_{84}$ was intentionally mixed with the 115 kDa, $Au_{\sim 500}$ species.[22] The ESI-MS results[22] of this mixture summarized here again in Figure S2 show a fwhm of 23 *m/z* for the $Au_{329}(SR)_{84}$ species, while the fwhm of 800 *m/z* was observed for $Au_{\sim 500}$ species. On the basis of these results, we conclude that a transition from a nanomolecule (*i.e.*, $Au_{329\pm0}(SR)_{84\pm0}$) to a polydisperse nature (*i.e.*, $Au_{500\pm10}(SR)_{120\pm3}$) occurs (also see Scheme 1c). We were unable to perform this experiment for $Au_{\sim 940}$ species due to limited sample availability. However, the trend of larger polydispersity as the size increases in phenylethanethiol-protected gold nanoparticles, namely, 25 ± 0, 38 ± 0, 144 ± 0, 329 ± 0, 500 ± 10, and 940 ± 20 Au atom is consistent with earlier results.

Atomic Pair Distribution Function Analysis. Atomic pair distribution function is the sum of the interatomic distances associated with each pair of atoms within the nanoparticle.[23−26] However, the Au−Au atom correlations are dominant due to the higher scattering function associated with the Au atom when compared with sulfur or carbon atoms. Figure 2 shows the synchrotron high-energy X-ray-based pair distribution function analysis of $Au_{\sim 940}(SR)_{\sim 160}$ nanoparticles, in comparison with commercially available fcc-like 100 nm gold nanoparticles. The calculated atomic PDF of other structural models of related size, such as the icosahedral Au_{923}, Marks decahedral Au_{831}, and truncated octahedral Au_{807}, is also included.[27] Clearly, the icosahedral model PDF patterns are significantly different than that of the experimental PDF pattern, suggesting that the core of Faradaurate-940 does not have an icosahedral arrangement. However, the PDF of Marks decahedron, truncated octahedral, and the 100 nm fcc-like naked Au nanoparticle (Sigma-Aldrich) all are closely related. Figure S3 shows the comparison of the experimental PDF of Faradaurate-940 with that of the 100 nm fcc-like Au nanoparticle in the 0−12 Å region. So from real space atomic PDF pattern also, it is not possible to distinguish between decahedral *versus* truncated octahedral/fcc atomic arrangements. Figure S4 shows the reciprocal space, intensity *versus* *Q* plot of Faradaurate-940.

Scanning Transmission Electron Microscopy Analysis. Figure 3a,b shows the low-magnification STEM images of ensemble of particles (1000s per frame), displaying the monodispersity of the particles. Furthermore, the atomic structure was studied in high-resolution STEM images. Atomic resolution high-angle annular dark-field (HAADF)-STEM images show the fcc-like, 2.9 ± 0.1 nm nanoparticles. Figure 3c−i shows the representative atomic resolution images of the $Au_{\sim 940}(SR)_{\sim 160}$. Figure 3j shows the FFT of the particle in 3i. The measured lattice spacings are very close to that of bulk fcc Au. Faceting is also regularly observed in the atomic resolution images, as would be expected based on the PDF analysis, which indicated fcc-truncated octahedra or Marks decahedra as possible structures for the $Au_{\sim 940}(SR)_{\sim 160}$ nanocrystals. However, the unique features observed in atomic resolution images and simulations of Marks decahedron (or icosahedron) reported in the literature[28] were not observed here. Further, HAADF-STEM images of the $Au_{\sim 940}(SR)_{\sim 160}$ nanocrystals presented here are consistent with previously reported, simulated STEM images of truncated octahedral clusters.[28,29] Thus, STEM imaging strongly suggests a fcc-truncated octahedral structure, while also confirming the monodispersity of this material.

Small-Angle X-ray Scattering. Figure 4a presents the SAXS data of $Au_{\sim 940}(SR)_{\sim 160}$. Since the molecular weight is roughly proportional to the cube of molecular size, the narrow molecular weight dispersion (<±2%) measured above for Au_{940} implies that its size falls in an even narrower dispersion (*i.e.*, <±1%). This near monodispersion of size was further supported by the wide range of linear Guinier behavior ($\ln[I(q)]$ *vs* q^2, Figure 4a inset) and the strong oscillating features in the *q* range of 0.2−0.6 $Å^{-1}$. The SAXS Guinier fit (*i.e.*, $\ln[I(q)] = \ln[I(q = 0)] - R_g^2q^2/3$ at *q* close to zero) provides the radius of gyration, R_g, of 1.32 ± 0.07 nm. The pair distance distribution function that is the inverse Fourier transform of the SAXS profile and essentially a weighted population histogram of atom pair distances displays a Gaussian shape (Figure 4b), indicating that the particle

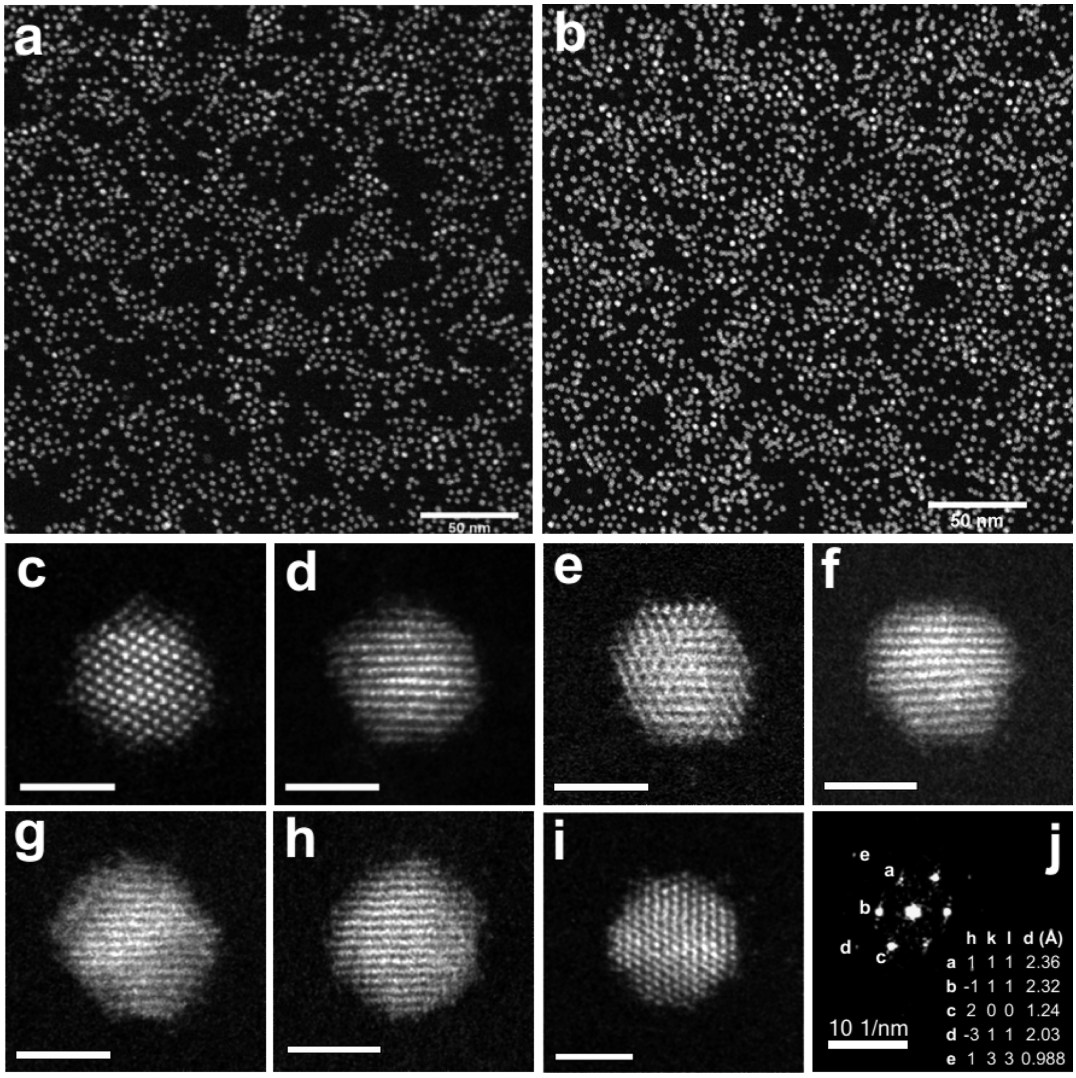

Figure 3. Electron microscopy. STEM images of the $Au_{\sim 940}(SR)_{\sim 160}$ nanoparticles. (a,b) Low-magnification STEM images. (c−i) High-resolution HAADF-STEM image of the individual nanoparticles, scale bar is 2 nm. (j) Fast Fourier transform of (i) showing lattice spots similar to bulk fcc Au oriented along the [0−11] zone axis.

adopts a globular form.[30] The three-dimensional molecular envelope derived from the SAXS data using an *ab initio* program DAMMIN[32] exhibits an ellipsoid-like shape, and its length is about 3.3 nm and the cross section about 2.5−2.8 nm, displayed in Figure 4c. It should be pointed out that, since the electron density of thiolate (SR) ligand is much less than that of the Au cluster core, the SAXS data and the molecular envelope are dominated by the contribution from the Au_{940} nanoparticle core. This SAXS molecular envelope is consistent with the STEM images, in terms of shape and size, and interestingly, it also shows facet features. In contrast to SAXS measuring the overall particle size, PDF only probes the size of the ordered domain within the particle, which is about 2.4 nm for Au_{940} showed in Figure 2. The size difference from SAXS and PDF measurements reflects the amount of disorder in the particle, most likely in the regions close to the surface. Compared to STEM measurements, the SAXS

TABLE 1. Properties of the $Au_{\sim 940}(SR)_{\sim 160}$ Faradaurate-940

composition	TEM diameter (nm)	powder XRD	PDF	optical data peak (nm), ε (M^{-1} cm^{-1})
$Au_{940\pm 20}(SR)_{160\pm 4}$	2.9 ± 0.1	fcc	fcc	~505, 1.58 × 10^6

represents an average of contributions from a statistically significant population of nanoparticles. For example, current SAXS data measured *ca.* 10^{12} individual nanoparticles in the beam path.

Structure Model. On the basis of PDF and STEM data, we propose the Au_{807} truncated octahedra model as the most probable structure for the metal core of the $Au_{\sim 940}$ nanoparticles. The Au_{923} cuboctahedral core model will allow only 17 Au atoms for the ligand interface, which can interact with a maximum of 34 ligands. However, the proposed Au_{807} TO model leaves 133 gold atoms, a reasonable number, to form a complete Au−SR

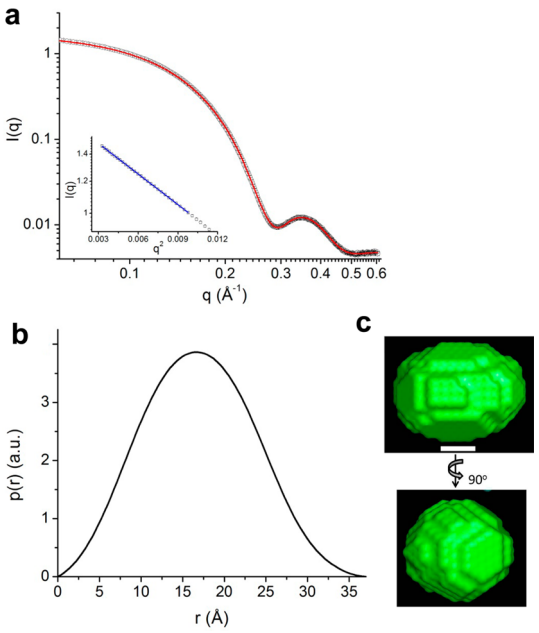

Figure 4. SAXS data, fittings, and the derived SAXS molecular envelope of Au_{940} nanoparticle. (A) SAXS data (black open circle with error bar) were collected up to 0.6 Å^{-1}. The red curve is a representative fitting in the molecular envelope calculation. The molecular envelope, also known as bead model, was calculated using the program DAMMIN, with SAXS data up to 0.6 Å^{-1}. The inset is the Guinier fit for SAXS data at q close to 0. R_g obtained from the fitting is 1.32 ± 0.07 nm. (B) Pair distance distribution function, p(r), derived from SAXS data in (A) using the program GNOM.[31] (C) Two views of the final SAXS molecular envelope. The length of the white bar is 1.0 nm. Twenty independent molecular envelope calculations were performed, and the resulting envelopes were further averaged to generate the final consensus molecular envelope.

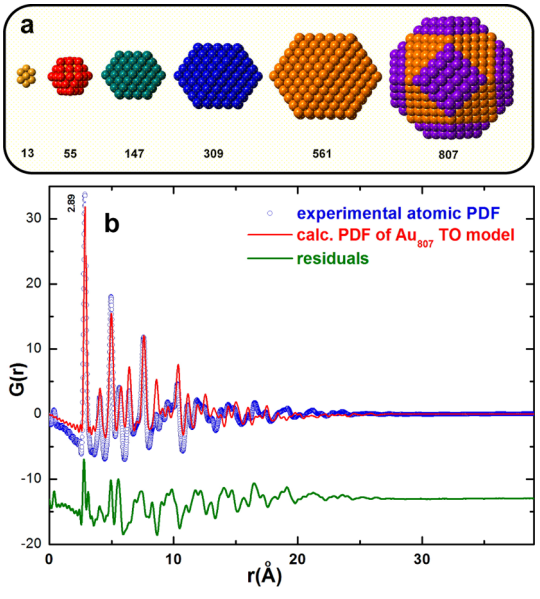

Figure 5. (a) Proposed six-shell Au_{807} atomic model for the metal-core-only portion of $Au_{\sim 940}(SR)_{\sim 160}$ nanoparticles. (b) PDF fit of the Au_{807} TO model with that of the experimental PDF of $Au_{\sim 940}(SR)_{\sim 160}$. The R_w is 44%. Note that the model only considers the metal core.

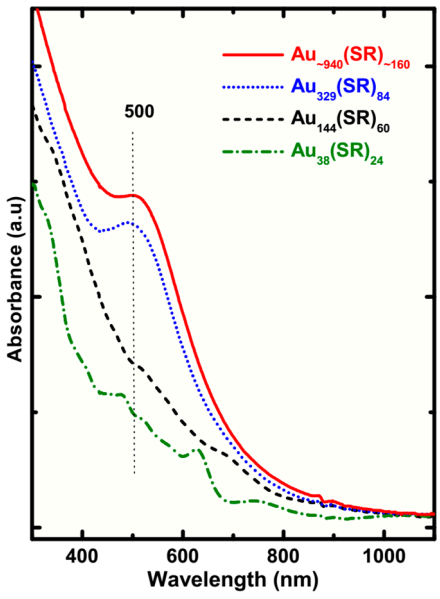

Figure 6. UV−vis−NIR spectra of $Au_{\sim 940}(SR)_{\sim 160}$ in comparison with $Au_{38}(SR)_{24}$, $Au_{144}(SR)_{60}$, and $Au_{329}(SR)_{84}$.

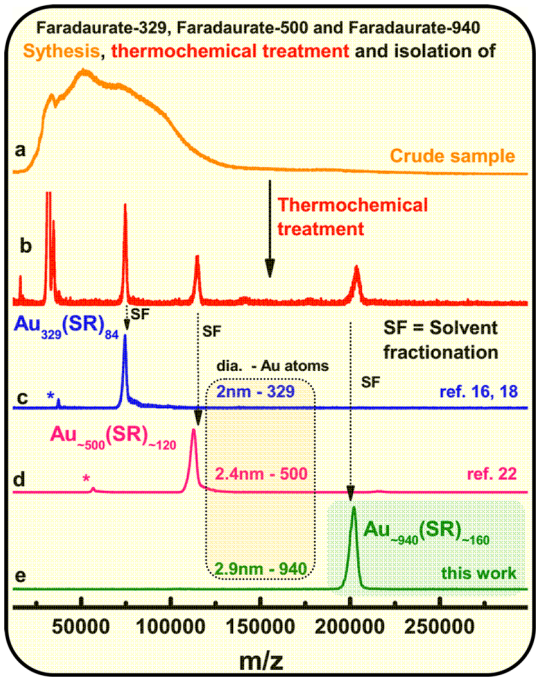

Figure 7. MALDI-MS of (a) crude product, (b) product after thermochemical treatment for 4 days, and isolation of (c) Faradaurate-329 ($Au_{329}(SR)_{84}$),[16,18] (d) Faradaurate-500 ($Au_{\sim 500}(SR)_{\sim 120}$),[22] and (e) Faradaurate-940 ($Au_{\sim 940}(SR)_{\sim 160}$) by solvent fractionation.[20] Refer to Scheme 2, Figure S5 and Experimental Section. Asterisk indicates 2+ charge states.

interface, supporting 160 thiolate ligands. Figure 5 shows the proposed six shells of Au_{807}-truncated octahedron core for $Au_{940}(SR)_{160}$. The model consists of 13, 42, 92, 162, 252, and 246 atoms in each shell. Using PDFgui, PDF fitting was performed for the Au_{807} TO model with that of the experimental PDF data of $Au_{\sim 940}(SR)_{\sim 160}$.[33] The residual R_w value of 44% is high, but this

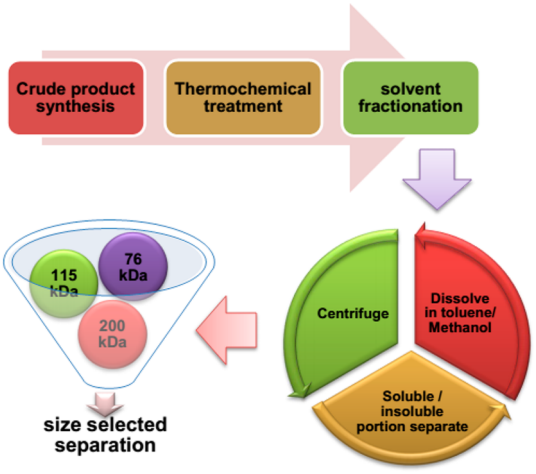

Scheme 2. Synthesis and isolation of Faradaurate- 940: The synthesis was carried out in three steps. Crude nanoparticles mixtures were synthesized according to an earlier report with minor modification.[16] Then thermochemical treatment was conducted to narrow down the size distribution and remove the metastable nanoparticles. Finally solvent fractionation[20] was continued to isolate the pure $Au_{\sim 940}(SR)_{\sim 160}$.

can in part be explained by the fact that we only considered the metal core of Au_{807} and the remaining ~140 atoms in the interface are omitted. Clearly, future studies on detailed atomic structure is warranted and is beyond the scope of this first report on the discovery of $Au_{\sim 940}(SR)_{\sim 160}$.

Figure 6 shows the UV−vis−NIR spectra of the $Au_{\sim 940}(SR)_{\sim 160}$ plasmonic nanoparticles in comparison with molecule-like $Au_{38}(SR)_{24}$ (green), quantized double layer charging $Au_{144}(SR)_{60}$ (black), and plasmonic[16,34] $Au_{329}(SR)_{84}$ (blue). Surface plasmon resonance of $Au_{\sim 940}(SR)_{\sim 160}$ is not sharp, but rather exhibits a characteristically broad spectrum when compared to $Au_{329}(SR)_{84}$. This may be due to averaging effects, where several resonance frequencies of different nanoparticle compositions present in the sample are averaged. According to the composition, $Au_{\sim 940}(SR)_{\sim 160}$ plasmon resonance is supported by (940 − 160 =) ~780 free electrons.

Table 1 summarizes the properties of $Au_{\sim 940}(SR)_{\sim 160}$ nanoparticles determined by a comprehensive set of analytical tools. Pair distribution function analysis and powder XRD shows the fcc-like atomic arrangement.

Figure 7a shows the mass spectrum of the crude product obtained in step 1. Figure 7b shows the mass spectrum of the product after the thermochemical treatment in step 2. This spectra shows how the sample with the broad mass spectrum is reduced to a few major, highly stable species, including the 329−, ~500− and ~940− atom species. Figure 7c−e shows the products obtained during the solvent fractionation purification process described in step 3 and Scheme 2. The interesting aspect of this Figure 7b and Figure S5 is the presence of ultrasmall Au_{25} and Au_{38} nanomolecules, then the middle mass range contains Au_{130} and Au_{144} nanomolecules, followed by the plasmonic 76.3, 115, and 200 kDa nanoparticles all in one synthetic batch. In this report, we mainly focus on the 200 kDa nanoparticles which were isolated using the method shown in Scheme 2.

High Stability. The $Au_{\sim 940}(SR)_{\sim 160}$ nanoparticles are *highly stable* upon prolonged thermochemical treatment at 80 °C for 7 to 10 days. These are ultrastable as shown by their stability under ambient environmental conditions in dry form and in solution and can be dried and redispersed in organic solvents without a change in its physicochemical properties.

CONCLUSION

In this work, we report the composition of 200 kDa nanocrystals to be $Au_{940\pm 20}(SCH_2CH_2Ph)_{160\pm 4}$. This is the first instance in which ESI-MS mass spectrometry was used to determine composition of thiolated gold nanoparticles to the atomic level, at such high mass, namely, the 200 kDa mass range. HAADF-STEM (2.9 ± 0.1 nm) and SAXS (3.0 ± 0.2 nm) size measurements show good agreement and both show monodisperse $Au_{\sim 940}(SR)_{\sim 160}$ nanoparticles. The plasmonic behavior of the title nanocrystals with a molecular composition may open the door for potential applications in sensors, solar cells, catalysis, and nano-optical devices.

EXPERIMENTAL SECTION

Synthesis of $Au_{\sim 940}(SR)_{\sim 160}$ nanoparticles was conducted in three steps. Crude nanoparticle mixtures were synthesized using our early report with modification.[16] Then thermochemical treatment was conducted to narrow down the size distribution and remove the metastable nanoparticles.[35,36] Finally, solvent fractionation was continued to isolate the pure $Au_{\sim 940}(SR)_{\sim 160}$. These steps and their corresponding mass spectra are shown in Scheme 2 and Figure 7, respectively.

Step 1: A mixture of $HAuCl_4$ (0.9 mmol in 30 mL of distilled water) and tetraoctylammonium bromide (1.1 mmol in 30 mL of toluene) was stirred in a 500 mL round-bottom flask. After 30 min, phenylethanethiol (gold to thiol ratio was maintained at 1:0.25) was added and stirred for another 30 min. Then the solution mixture was cooled to 0 °C, while stirring was continued for another 30 min. Then the ice-cold solution of $NaBH_4$ (10 mmol) was added, and reaction was continued for 2 h at 0 °C. Then, the aqueous layer was decanted, and the organic layer was removed by rotary evaporation. This mixture was washed with methanol to remove excess thiol and other byproducts.

Step 2: The crude product (200 mg) from step 1 was dissolved in toluene (1 mL) and subjected to thermochemical treatment with excess phenylethanethiol (1 mL) at 90 °C for several days (4−9 days), while the experiment was monitored with MALDI-MS. Then, the product was washed with methanol several times to remove excess thiol and extracted with toluene.

Step 3: The final product contains several nanoparticles including the 76.3,[16,18] 115,[22] and 200 kDa. Solvent fractionation[20] was continued using toluene/methanol mixture until 200 kDa nanoparticles were isolated in pure form.

Characterization. *Mass Spectrometric Analysis.* MALDI-MS was recorded using Bruker AutoFlex 1, and data analysis was done using Bruker Flex analysis 3.0. Samples were mixed with DCTB matrix,[19] and data were acquired from 4−500 kDa mass range. ESI-MS data was acquired using a Waters SYNAPT Q-TOF HDMS instrument. Nanoparticles were mixed with 50:50 toluene/CH_3CN or 50:50 THF/CH_3CN solvent system for analysis. $Au_{25}(SCH_2CH_2Ph)_{18}$ and $Au_{144}(SCH_2CH_2Ph)_{60}$ were used for calibration check.

Synchrotron X-ray and Pair Distribution Function Analysis. The total scattering data were collected using synchrotron X-rays at beamline 11-ID-B at the Advanced Photon Source at Argonne National Laboratory. The samples were loaded in polyimide tubing (~1 mm diameter), and a large area detector (PerkinElmer a-Si) was combined with high-energy X-rays (E = ~58 keV, λ = 0.21218 Å) to collect data to high values of momentum transfer (Q). Fit2d was used to reduce the two-dimensional images to one-dimensional diffraction data as a function of Q. The data were corrected for background and Compton scattering within pdfgetX2.[33,37] Fourier transform of the data to Q_{max} = 22 $Å^{-1}$ gave the PDFs, $G(r)$. The calculated atomic PDF and PDF fitting was performed using PDFgui.[33]

Small-Angle X-ray Scattering. The SAXS measurements were performed at the 12-ID-B beamline of APS using 12 keV X-ray energy. The SAXS data were collected with a Pilatus 2 M detector (DECTRIS Ltd.), and cutoff energy was set as 10 keV to eliminate possible fluorescence background. The beam size with 0.05 × 0.2 mm^2 and exposure times of 1 s were used for the measurement. The data were fully corrected, reduced to intensity *versus* scattering vector (q) profiles, and background-subtracted using the software package at the beamline.

Scanning Transmission Electron Microscopy Analysis. STEM samples were prepared by drop-casting a toluene solution of nanoparticle suspension onto lacey carbon films supported on 3 mm Cu grids. HAADF-STEM images were acquired in a JEOL JEM-2200FS with a CEOS aberration corrector on the probe-forming system. Because the particles proved to be sensitive to the electron beam, images were recorded with electron doses below 5 × 10^4 $e^-/Å^2$. High-resolution STEM images were processed using a smoothing spatial filter built into the Gatan Microscopy Suite. At higher magnification, neighboring particles were prone to rapid necking and coalescence. Thus, for particle counting analysis, areas of well-separated particles were chosen, and coalesced particles were excluded from the counting statistics. While cooling the particles in a cryogenic holder did show some improvement in particle stability, this method was not routinely used to obtain images for particle counts. Images were analyzed using ImageJ software (version 1.46r).

Optical Absorption Spectroscopy. UV−visible−NIR absorption spectra were recorded using Shimadzu UV-1601 spectrometer in toluene in the 300−1100 nm range.

Conflict of Interest: The authors declare no competing financial interest.

Acknowledgment. C.K. and A.D. gratefully acknowledge support from NSF CHE-1255519. We thank Karena Chapman for collecting PDF data and Ferrando Riccardo for the coordinates of the structure models. Work performed at Argonne and the use of the Advanced Photon Source, an Office of Science User Facility operated for the U.S. Department of Energy (DOE) Office of Science by Argonne National Laboratory, was supported by the U.S. DOE under Contract No. DE-AC02-06CH11357. Electron microscopy research was supported through a user project supported by ORNL's Center for Nanophase Materials Sciences (CNMS), which is sponsored by the Scientific User Facilities Division, Office of Basic Energy Sciences, U.S. Department of Energy.

Supporting Information Available: Additional mass spectrometry and X-ray diffraction data. This material is available free of charge *via* the Internet at http://pubs.acs.org.

REFERENCES AND NOTES

1. Heaven, M. W.; Dass, A.; White, P. S.; Holt, K. M.; Murray, R. W. Crystal Structure of the Gold Nanoparticle $[N(C_8H_{17})_4][Au_{25}(SCH_2CH_2Ph)_{18}]$. *J. Am. Chem. Soc.* **2008**, *130*, 3754–3755.
2. Dolamic, I.; Knoppe, S.; Dass, A.; Bürgi, T. First Enantioseparation and Circular Dichroism Spectra of Au_{38} Clusters Protected By Achiral Ligands. *Nat. Commun.* **2012**, *3*, 798.
3. Knoppe, S.; Dolamic, I.; Dass, A.; Bürgi, T. Separation of Enantiomers and CD Spectra of $Au_{40}(SCH_2CH_2Ph)_{24}$: Spectroscopic Evidence for Intrinsic Chirality. *Angew. Chem., Int. Ed.* **2012**, *51*, 7589–7591.
4. Negishi, Y.; Sakamoto, C.; Ohyama, T.; Tsukuda, T. Synthesis and the Origin of the Stability of Thiolate-Protected Au_{130} and Au_{187} Clusters. *J. Phys. Chem. Lett.* **2012**, *3*, 1624–1628.
5. Fields-Zinna, C. A.; Sardar, R.; Beasley, C. A.; Murray, R. W. Electrospray Ionization Mass Spectrometry of Intrinsically Cationized Nanoparticles, $[Au_{144/146}(SC_{11}H_{22}N(CH_2CH_3)_3^+)_x(S(CH_2)_5CH_3)_y]^{x+}$. *J. Am. Chem. Soc.* **2009**, *131*, 16266–16271.
6. Templeton, A. C.; Wuelfing, W. P.; Murray, R. W. Monolayer-Protected Cluster Molecules. *Acc. Chem. Res.* **1999**, *33*, 27–36.
7. Antonello, S.; Perera, N. V.; Ruzzi, M.; Gascón, J. A.; Maran, F. Interplay of Charge State, Lability, and Magnetism in the Molecule-like $Au_{25}(SR)_{18}$ Cluster. *J. Am. Chem. Soc.* **2013**, *135*, 15585–15594.
8. Kumara, C.; Dass, A. $(AuAg)_{144}(SR)_{60}$ Alloy Nanomolecules. *Nanoscale* **2011**, *3*, 3064–3067.
9. Negishi, Y.; Kurashige, W.; Niihori, Y.; Nobusada, K. Toward the Creation of Stable, Functionalized Metal Clusters. *Phys. Chem. Chem. Phys.* **2013**, *15*, 18736–18751.
10. Jupally, V. R.; Kota, R.; Dornshuld, E. V.; Mattern, D. L.; Tschumper, G. S.; Jiang, D.-E.; Dass, A. Interstaple Dithiol Cross-Linking in $Au_{25}(SR)_{18}$ Nanomolecules: A Combined Mass Spectrometric and Computational Study. *J. Am. Chem. Soc.* **2011**, *133*, 20258–20266.
11. Heinecke, C. L.; Ni, T. W.; Malola, S.; Mäkinen, V.; Wong, O. A.; Häkkinen, H.; Ackerson, C. J. Structural and Theoretical Basis for Ligand Exchange on Thiolate Monolayer Protected Gold Nanoclusters. *J. Am. Chem. Soc.* **2012**, *134*, 13316–13322.
12. Jadzinsky, P. D.; Calero, G.; Ackerson, C. J.; Bushnell, D. A.; Kornberg, R. D. Structure of a Thiol Monolayer-Protected Gold Nanoparticle at 1.1 Å Resolution. *Science* **2007**, *318*, 430–433.
13. Chen, Y.; Palmer, R. E.; Wilcoxon, J. P. Sintering of Passivated Gold Nanoparticles under the Electron Beam. *Langmuir* **2006**, *22*, 2851–2855.
14. Hostetler, M. J.; Wingate, J. E.; Zhong, C.-J.; Harris, J. E.; Vachet, R. W.; Clark, M. R.; Londono, J. D.; Green, S. J.; Stokes, J. J.; Wignall, G. D.; *et al.* Alkanethiolate Gold Cluster Molecules with Core Diameters from 1.5 to 5.2 nm: Core and Monolayer Properties as a Function of Core Size. *Langmuir* **1998**, *14*, 17–30.
15. Whetten, R. L.; Khoury, J. T.; Alvarez, M. M.; Murthy, S.; Vezmar, I.; Wang, Z. L.; Stephens, P. W.; Cleveland, C. L.; Luedtke, W. D.; Landman, U. Nanocrystal Gold Molecules. *Adv. Mater.* **1996**, *8*, 428–433.
16. Dass, A. Faradaurate Nanomolecules: A Superstable Plasmonic 76.3 kDa Cluster. *J. Am. Chem. Soc.* **2011**, *133*, 19259–19261.
17. Faraday, M. The Bakerian Lecture: Experimental Relations of Gold (and Other Metals) to Light. *Philos. Trans. R. Soc. London* **1857**, *147*, 145–181.
18. Kumara, C.; Dass, A. $Au_{329}(SR)_{84}$ Nanomolecules: Compositional Assignment of the 76.3 kDa Plasmonic Faradaurates. *Anal. Chem.* **2014**, *86*, 4227–4232.
19. Dass, A.; Stevenson, A.; Dubay, G. R.; Tracy, J. B.; Murray, R. W. Nanoparticle MALDI-TOF Mass Spectrometry without Fragmentation: $Au_{25}(SCH_2CH_2Ph)_{18}$ and Mixed Monolayer $Au_{25}(SCH_2CH_2Ph)_{18-x}(L)_x$. *J. Am. Chem. Soc.* **2008**, *130*, 5940–5946.
20. Nimmala, P. R.; Yoon, B.; Whetten, R. L.; Landman, U.; Dass, A. $Au_{67}(SR)_{35}$ Nanomolecules: Characteristic Size-Specific Optical, Electrochemical, Structural Properties and First-Principles Theoretical Analysis. *J. Phys. Chem. A* **2013**, *117*, 504–517.
21. Chaki, N. K.; Negishi, Y.; Tsunoyama, H.; Shichibu, Y.; Tsukuda, T. Ubiquitous 8 and 29 kDa Gold:Alkanethiolate Cluster Compounds: Mass-Spectrometric Determination

of Molecular Formulas and Structural Implications. *J. Am. Chem. Soc.* **2008**, *130*, 8608–8610.
22. Kumara, C.; Zuo, X.; Ilavsky, J.; Chapman, K. W.; Cullen, D. A.; Dass, A. Super-Stable, Highly Monodisperse Plasmonic Faradaurate-500 Nanocrystals with 500 Gold Atoms: $Au_{\sim 500}(SR)_{\sim 120}$. *J. Am. Chem. Soc.* **2014**, *36*, 7410–7417.
23. Egami, T.; Billinge, S. J. L. *Underneath the Bragg Peaks: Structural Analysis of Complex Materials*; Elsevier: Oxford, UK, 2012.
24. Billinge, S. J. L.; Kanatzidis, M. G. Beyond Crystallography: The Study of Disorder, Nanocrystallinity and Crystallographically Challenged Materials with Pair Distribution Functions. *Chem. Commun.* **2004**, 749–760.
25. Yang, L.; Shan, S.; Loukrakpam, R.; Petkov, V.; Ren, Y.; Wanjala, B. N.; Engelhard, M. H.; Luo, J.; Yin, J.; Chen, Y.; *et al.* Role of Support−Nanoalloy Interactions in the Atomic-Scale Structural and Chemical Ordering for Tuning Catalytic Sites. *J. Am. Chem. Soc.* **2012**, *134*, 15048–15060.
26. Petkov, V. Pair Distribution Functions Analysis. In *Characterization of Materials*; John Wiley & Sons: New York, 2002.
27. Baletto, F.; Ferrando, R. Structural Properties of Nanoclusters: Energetic, Thermodynamic, and Kinetic Effects. *Rev. Mod. Phys.* **2005**, *77*, 371–423.
28. Wang, Z. W.; Palmer, R. E. Determination of the Ground-State Atomic Structures of Size-Selected Au Nanoclusters by Electron-Beam-Induced Transformation. *Phys. Rev. Lett.* **2012**, *108*, 245502-5.
29. Wang, Z. W.; Palmer, R. E. Mass Spectrometry and Dynamics of Gold Adatoms Observed on the Surface of Size-Selected Au Nanoclusters. *Nano Lett.* **2012**, *12*, 91–95.
30. Walenta, E. Small Angle X-ray Scattering. *Acta Polym.* **1985**, *36*, 296–296.
31. Svergun, D. Determination of the Regularization Parameter in Indirect-Transform Methods Using Perceptual Criteria. *J. Appl. Crystallogr.* **1992**, *25*, 495–503.
32. Svergun, D. I. Restoring Low Resolution Structure of Biological Macromolecules from Solution Scattering Using Simulated Annealing. *Biophys. J.* **1999**, *76*, 2879–2886.
33. Qiu, X.; Bozin, E. S.; Juhas, P.; Proffen, T.; Billinge, S. J. L. Reciprocal-Space Instrumental Effects on the Real-Space Neutron Atomic Pair Distribution Function. *J. Appl. Crystallogr.* **2004**, *37*, 110–116.
34. Qian, H.; Zhu, Y.; Jin, R. Atomically Precise Gold Nanocrystal Molecules with Surface Plasmon Resonance. *Proc. Natl. Acad. Sci. U.S.A.* **2012**, *109*, 696–700.
35. Nimmala, P. R.; Jupally, V. R.; Dass, A. Core Size Conversion: Route for Exclusive Synthesis of Au_{38} or Au_{40} Nanomolecules. *Langmuir* **2014**, *30*, 2490–2497.
36. Schaaff, T. G.; Whetten, R. L. Controlled Etching of Au:SR Cluster Compounds. *J. Phys. Chem. B* **1999**, *103*, 9394–9396.
37. Chupas, P. J.; Qiu, X.; Hanson, J. C.; Lee, P. L.; Grey, C. P.; Billinge, S. J. L. Rapid-Acquisition Pair Distribution Function (RA-PDF) Analysis. *J. Appl. Crystallogr.* **2003**, *36*, 1342–1347.